PAX9 Determines Epigenetic State Transition and Cell Fate in Cancer

Zibo Zhao[1,2,3], Aileen P. Szczepanski[1,2,3], Natsumi Tsuboyama[1,2,3], Hiam Abdala-Valencia[4], Young Ah Goo[1,2,5], Benjamin D. Singer[1,2,4], Elizabeth T. Bartom[1,2,3], Feng Yue[1,2,3], and Lu Wang[1,2,3]

ABSTRACT

Abnormalities in genetic and epigenetic modifications can lead to drastic changes in gene expression profiles that are associated with various cancer types. Small cell lung cancer (SCLC) is an aggressive and deadly form of lung cancer with limited effective therapies currently available. By utilizing a genome-wide CRISPR-Cas9 dropout screen in SCLC cells, we identified paired box protein 9 (PAX9) as an essential factor that is overexpressed in human malignant SCLC tumor samples and is transcriptionally driven by the BAP1/ASXL3/BRD4 epigenetic axis. Genome-wide studies revealed that PAX9 occupies distal enhancer elements and represses gene expression by restricting enhancer activity. In multiple SCLC cell lines, genetic depletion of *PAX9* led to significant induction of a primed-active enhancer transition, resulting in increased expression of a large number of neural differentiation and tumor-suppressive genes. Mechanistically, PAX9 interacted and cofunctioned with the nucleosome remodeling and deacetylase (NuRD) complex at enhancers to repress nearby gene expression, which was reversed by pharmacologic HDAC inhibition. Overall, this study provides mechanistic insight into the oncogenic function of the PAX9/NuRD complex epigenetic axis in human SCLC and suggests that reactivation of primed enhancers may have potential therapeutic efficacy in treating SCLC expressing high levels of PAX9.

Significance: A genome-wide screen in small cell lung cancer reveals PAX9/NuRD-mediated epigenetic enhancer silencing and tumor progression, supporting the development of novel personalized therapeutic approaches targeting the PAX9-regulated network.

Introduction

Lung cancer is the leading cause of cancer deaths in men and the second leading cause of cancer deaths in women worldwide (1). Lung cancer is classified as small cell lung carcinoma (SCLC; around 13%) or non–small cell lung carcinoma (NSCLC; around 83% of cases; ref. 2). The 5-year survival for SCLC (6%) is lower compared with NSCLC (23%) for all stages combined as well as for each stage. SCLC is characterized as being more aggressive and a deadlier form of lung cancer with a predisposition for rapid growth, early metastasis, and acquired therapeutic resistance (3, 4).

Emerging studies from primary human SCLC tumors, patient-derived xenografts, cancer cell lines, and genetically engineered mouse models appear to be converging on a new model of SCLC subtypes defined by the differential expression of four key transcription regulators: achaete-scute homolog 1 (*ASCL1*), neurogenic differentiation factor 1 (*NEUROD1*), yes-associated protein 1 (*YAP1*), and POU class 2 homeobox 3 (*POU2F3*; ref. 5). The A-subtype SCLC is defined by *ASCL1*, the most abundant (∼70%) of all the human SCLC subtypes (6). ASCL1 is a lineage-specific transcription factor that directly regulates the expression of genes involved in SCLC tumor growth (7–10). In addition, ASCL1 is required for neuroendocrine (NE) tumor formation in the *Rb/p53/p130* mutant mouse model (11). To date, it still remains unknown as to what each subtype's molecular features are and whether these subtypes respond differently to specific treatments. Therefore, discovering the functional biomarkers for each subtype is critical for understanding the molecular basis underlying SCLC tumorigenesis and in guiding the clinical treatment for patients with SCLC.

Dysregulations and mutations within epigenetic factors, such as histone lysine methyltransferases (12–14), deubiquitinases (15), DNA methyltransferases (16), and DNA demethylases (17), are all common mechanisms of tumorigenesis. Emerging pieces of evidence have shown that SCLC carcinogenesis may be driven by these epigenetic processes (4, 18, 19). Our previous studies have identified and characterized an SCLC-specific additional sex combs-like protein, ASXL3, which is the largest subunit within the Polycomb repressive deubiquitinase (PR-DUB) complex, or also known as the BAP1 complex (20). Interestingly, ASXL3 defines the SCLC-A subtype tumors independent of ASCL1. Mechanistically, the chromatin bound ASXL3 functions as an adaptor protein, which directly connects BRD4 to the BAP1/ASXL3 complex and maintains chromatin occupancy of the functional BAP1/ASXL3/BRD4 epigenetic axis at active enhancers (20). However, how ASXL3 maintains cell viability and how the BAP1/ASXL3/BRD4 epigenetic axis determines cell fate remains to be discovered. In our current studies, by utilizing genome-wide CRISPR-Cas9 screening and unbiased genetic/epigenetic approaches, we have identified the primary transcriptional targets of ASXL3 in multiple SCLC cells and further uncovered the mechanisms as to how transitions made in the status of enhancers determine gene expression and cell viability in SCLC.

[1]Department of Biochemistry and Molecular Genetics, Feinberg School of Medicine, Northwestern University, Chicago, Illinois. [2]Simpson Querrey Center for Epigenetics, Feinberg School of Medicine, Northwestern University, Chicago, Illinois. [3]Robert H. Lurie Comprehensive Cancer Center, Feinberg School of Medicine, Northwestern University, Chicago, Illinois. [4]Division of Pulmonary and Critical Care Medicine, Department of Medicine, Feinberg School of Medicine, Northwestern University, Chicago, Illinois. [5]Proteomics Center of Excellence, Northwestern University, Evanston, Illinois.

Z. Zhao and A.P. Szczepanski contributed equally to this article.

Corresponding Author: Lu Wang, Biochemistry and Molecular Genetics, Northwestern University, Chicago, IL 60611. E-mail: lu.wang1@northwestern.edu

Cancer Res 2021;81:4696–708

doi: 10.1158/0008-5472.CAN-21-1114

Materials and Methods

Cell lines

HEK293T cells were obtained from ATCC, and then maintained with DMEM (Gibco) containing 10% FBS (Sigma). The SCLC cell lines were obtained from ATCC. NCI-H748, NCI-H1963, NCI-H69, NCI-H889, NCI-H196, NCI-H226, and NCI-H209 cells were maintained with ATCC-formulated RPMI1640 medium containing 10% FBS (Sigma). NCI-H1882, NCI-H1105, and NCI-H2171 cells were maintained with ATCC-formulated DMEM/F12 cell culture media containing 10% FBS (Sigma). All cell lines were authenticated through STR profiling and tested bi-weekly for *Mycoplasma* by PCR. Cell lines were not passaged more than 20 times.

Genome-wide CRISPR screening

SCLC cells were transduced with lentiviruses expressing the GeCKO CRISPR library A and library B (21), which contains 123,411 gRNAs targeting 19,050 genes. The A and B libraries contain six sgRNAs per gene (three sgRNAs in each library), and 1,000 control sgRNAs as well. Cells were infected with virus pools at multiplicity of infection = 0.3. Starting at 2 days postinfection, infected cells were selected in 2 μg/mL puromycin for 2 days. Surviving cells were then cultured without puromycin for 14 days before their genomic DNA was isolated, and amplified with primers as described previously (21).

IHC

Staining for PAX9 was performed with formalin-fixed, paraffin-embedded tumor microarrays, as we described previously (22). Details and references are provided in the Supplementary Materials and Methods.

Immunoprecipitation

The immunoprecipitation (IP) experiment was performed as described previously (20). Details and references are provided in the Supplementary Materials and Methods.

RNA interference, CRISPR, and real-time PCR

The cells were infected with lentivirus containing short-hairpin RNAs (shRNA) in the presence of 4 μg/mL polybrene (Sigma) for 24 hours in RPMI1640 supplemented with 10% FBS. The shRNA constructs were purchased from Sigma. The clone IDs for PAX9 are TRCN0000274075 (sh*PAX9*–1), TRCN0000285142 (sh*PAX9*–2), and TRCN0000020381 (sh*PAX9*–3). The nontargeting (sh*Ctrl*) shRNA construct (SHC002) was purchased from Sigma. The infected cells were selected with 2 μg/mL puromycin for an additional 48 hours. Oligo sequences used in this manuscript were listed in the Supplementary Table S1.

RNA-seq

The RNA-seq experiment was performed as described previously (20). Paramagnetic beads coupled with oligo d(T) are combined with total RNA to isolate poly(A)+ transcripts based on NEBNext Poly(A) mRNA Magnetic Isolation Module manual. All remaining steps for library construction were used according to the NEBNext Ultra II RNA Nondirectional Library Prep Kit from Illumina. Illumina 8-nt dual-indices. Samples were pooled and sequenced on a HiSeq with a read length configuration of 150 PE. Details and references are provided in the Supplementary Materials and Methods.

Chromatin immunoprecipitation sequencing assay

Chromatin immunoprecipitation sequencing (ChIP-seq) was performed as described previously (20). Briefly, the cells were harvested, fixed, and lysed with our standard protocol. For histone H3K27ac ChIP-seq analysis, 5% of chromatin from drosophila S2 cells were added as a spike-in control. All the peaks were called with the MACS v2.1.2 software using default parameters and corresponding input samples. Details and references are provided in the Supplementary Materials and Methods.

ATAC-seq

Frozen cells were thawed and the nuclei were harvested and subjected to tagmentation. The tagmentated DNA was further amplified with barcode primers, and sequenced on an Illumina HiSeq (Illumina) with a read length configuration of 150 PE for 50M PE reads (25M in each direction) per sample. Details and references are provided in the Supplementary Materials and Methods.

Mouse experiments

All mouse work was performed in accordance with protocols approved by The Center for Comparative Medicine of Northwestern University. 5- to 6-week-old athymic nude mice were used for xenograft experiments. For tumor growth assays, 5.0×10^5 KP1 (mouse SCLC cell line) cells were inoculated into the right flank of nude mice. Tumor growth was monitored every 3 days, 2 weeks after inoculation.

Statistical analyses

For statistical analyses, GraphPad Prism 7, Microsoft Excel, and R were used. All data involving a statistical analysis being reported met the criteria to use the appropriate statistical tests; for the normal distribution of data, the empirical rule was used to infer the distribution. For growth curves and time-course, RNA-seq *t* tests were calculated between the AUC values. Statistical tests used are reported in the figure legends.

Data availability

NSG data generated for this study are available at the Gene Expression Omnibus (GEO) under accession number GSE164247.

Results

Genome-wide CRISPR-Cas9 screening identifies factors that are essential for ASXL3-highly expressed cells' viability

To study how the BAP1/ASXL3/BRD4 epigenetic axis maintains SCLC cell viability and determines cell fate, we sought in our current studies to globally identify the factors that are selectively essential for ASXL3-high expressing cells (SCLC-A). Consequently, it has been demonstrated that a complete depletion of ASXL3 is lethal for SCLC cells (20, 23). Hence, we introduced two neuroendocrine SCLC cell lines with different ASXL3 levels for the screening: NCI-H1963 (ASXL3-high) and NCI-H2171 (ASXL3-low) cells. As a typical SCLC-A type cell line, NCI-H1963 cells express high levels of ASCL1, ASXL3, and MYCL (**Fig. 1A**). In contrast, the SCLC-N type NCI-H2171 cell line is NEUROD1 positive, ASCL1/ASXL3 negative, and expresses a high level of MYC (**Fig. 1A**). MYCL and MYC have been demonstrated to be critical drivers in SCLC-A and SCLC-N cancer types, respectively (5). Thus, MYCL and MYC served as positive controls in our CRISPR-Cas9 dropout screenings as we identify essential factors for NCI-H1963 and NCI-H2171 cells, respectively. Both cell lines were then transduced with lentiviruses expressing the GeCKO CRISPR library (21), which contains 123,411 gRNAs targeting 19,050 genes (**Fig. 1B**). After confirming the quality of our CRISPR-Cas9 screening and observing an identical gRNA distribution pattern between the two cell lines (Supplementary Figs. S1A and S1B), as well

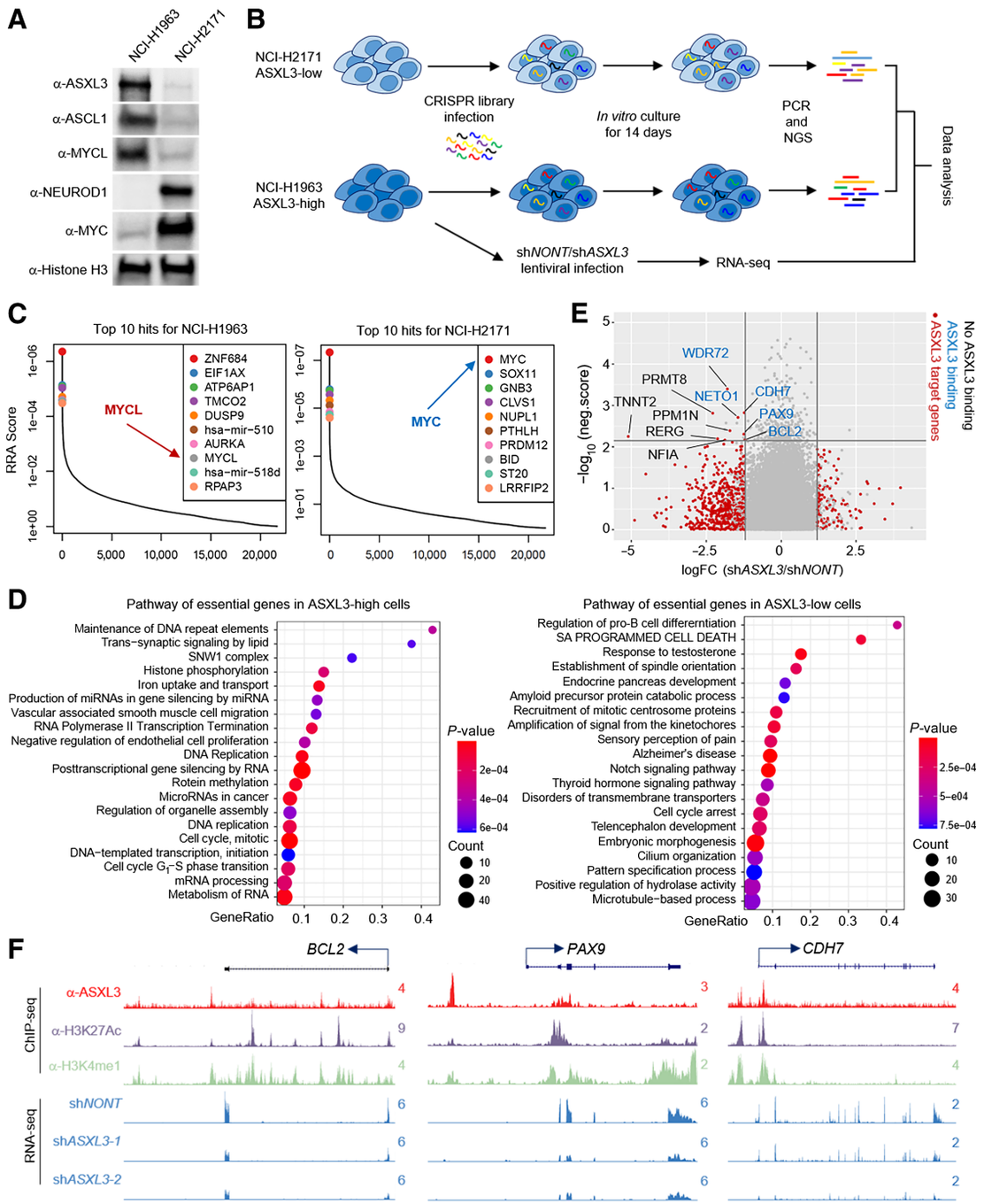

Figure 1.

Genome-wide CRISPR-CAS9 screen identifies factors that are essential for ASXL3 highly expressed cells' viability. **A,** The protein levels of ASXL3, ASCL1, MYCL, NEUROD1, and MYC were determined by Western blot analysis in NCI-H1963 (ASXL3-high) and NCI-H2171 (ASXL3-low) SCLC cells, with total histone H3 as a control. **B,** The method flowchart shows genome-wide CRISPR-Cas9 screening with GeCKO lentiviral gRNA library in NCI-H1963 and NCI-H2171 cells. **C,** Hockey stick plot representing the top 10 factors that are essential for ASXL3-high but not ASXL3-low (left) or ASXL3-low but not ASXL3-high (right) cells. **D,** Pathway analysis with Metascape of genes that are essential in either ASXL3-high or ASXL3-low cells. **E,** The scatter plot shows the genes that are transcriptional targets of ASXL3 and also essential for ASXL3-high expressing cell viability. *x*-axis, $\log_2$-fold change of gene expression with ASXL3 knockdown from RNA-seq; *y*-axis, negative $\log_{10}$ value of the negative RRA score from the CRISPR-Cas9 screening. **F,** Representative tracks showing the enhancer binding of ASXL3 at *BCL2, PAX9*, and *CDH7* gene loci, which contribute to active gene expression.

as a remarkable correlation between the two sublibraries (Supplementary Fig. S1C), we then applied the MAGeCK (24) algorithm to identify essential genes in both cell lines. As expected, *MYCL* and *MYC* were found among the top 10 genes essential for NCI-H1963 and NCI-H2171 cells, respectively (**Fig. 1C**). Compared with the ASXL3-lowly expressed NCI-H2171 cells, we found that the ASXL3-highly expressed NCI-H1963 cells were more sensitive to depletion of genes involved in pathways related to transcription and RNA metabolism (**Fig. 1D**).

To identify ASXL3 target genes that were also essential for ASXL3-highly expressed cells' viability, we performed an integration analyses of the genome-wide, CRISPR-Cas9 screening with the RNA-seq results using ASXL3 shRNA knockdown in NCI-H1963 cells. Overall, we have identified 103 ASXL3 target genes in NCI-H1963 cells that were essential for cell viability (Supplementary Fig. S1D). Interestingly, pathway analysis has identified a handful of neural differentiation and neural function pathways significantly enriched within this 103-gene signature (Supplementary Fig. S1E). The top 10 genes among the 103-gene signature include the following: *TNNT2, PRMT8, RERG, NFIA, PPM1N, WDR72, NETO1, CDH7, PAX9*, and *BCL2* (**Fig. 1E**; Supplementary Fig. S1F). We further validated the CRISPR screening results by performing a small-scaled validation with the top two CRISPR gRNA hits from each of the top ten gene signatures in both NCI-H1963 and NCI-H2171 cell lines (Supplementary Fig. S1G). On the basis of our ChIP-seq analysis, ASXL3 does not bind to all of these target genes listed here, suggesting that these genes might instead be indirect targets of ASXL3 (**Fig. 1E**). For the five direct target genes of ASXL3 (*WDR72, NETO1, CDH7, PAX9*, and *BCL2*), we detected a significant amount of enrichment for ASXL3 at the indicated enhancer regions (**Fig. 1F**; Supplementary Figs. S1H and S1I).

PAX9 is a potential biomarker of SCLC and is required for SCLC viability

It has been reported that there are significantly higher levels of ASXL3 expression in SCLC samples relative to a normal lung tissue sample by IHC staining, suggesting that ASXL3 could serve as a prognostic biomarker for human SCLC (23). To determine whether these 10 candidate genes are also involved in the clinical outcome of patients with SCLC, we first retrieved the RNA-seq data from a dataset that contains a total of 79 SCLC patients' tumor samples and 7 normal lung tissue samples (GSE60052; ref. 25). Then, we compared the gene expression profiles to determine the expression levels of those ten factors between normal and SCLC tissues. Consistent with previous reports, we found that there are significantly higher levels of ASXL3 expression in patient SCLC samples compared with normal lung tissue (P value = 8.2e−06; **Fig. 2A**). Intriguingly, we also found that two out of the ten candidate genes, *BCL2* (P-value = 1.56e−07) and *PAX9* (P-value = 4.24e−03), had expression levels that are significantly higher in SCLC tumor tissues versus normal tissue samples.

To determine whether there is a positive correlation between *BCL2, PAX9*, and *ASXL3* mRNA levels in the more diverse human SCLC cell lines, we compared the gene expression with RNA-seq results from 50 human SCLC cell lines (26). Overall, there was a trend representing all positive correlations between *ASXL3* versus *BCL2* and *PAX9* (**Fig. 2B**), and other essential factors (Supplementary Fig. S2A) within the 50 SCLC lung cancer cell lines. To further confirm the correlation between BCL2, PAX9, and ASXL3 at the protein level, we conducted a western blot using different SCLC cell lines with different ASXL3 expression levels. Consistent with the correlation revealed by mRNA levels, we found that there was also a strong proportional relationship between PAX9 and ASXL3 protein levels (**Fig. 2C**). Interestingly, there is no apparent correlation between BCL2 and ASXL3 at the protein level, suggesting that other factors may contribute to the BCL2 protein levels in SCLC. On the basis of previous studies, BCL2 is a known transcriptional target of the BAP1 complex (27) as well as BRD4 (28). This finding led us to test whether PAX9 could also be controlled by the BAP1/ASXL3/BRD4 epigenetic axis. Thus, we found that depletion of BAP1 by CRISPR-Cas9 (Supplementary Figs. S2B and S2C) or pharmaceutical inhibition of BRD4 (Supplementary Figs. S2D and S2E) resulted in a significant reduction in the expression of both *BCL2* and *PAX9*. In addition, both BAP1 and BRD4 were detected at active enhancers located near the *BCL2* and *PAX9* gene loci (Supplementary Fig. S2F). These results reveal a direct transcriptional control of *PAX9* expression by the BAP1/ASXL3/BRD4 epigenetic axis.

Then, we sought to introduce RNAi to validate our CRISPR-Cas9 screening result in different cell lines and determine whether the loss of PAX9 could affect different SCLC cells' viability *in vitro* and *in vivo*. As a result, we knocked down PAX9 with its specific shRNAs in NCI-H1963 (**Fig. 2D**) and NCI-H1882 cell lines (**Fig. 2E**), both of which express high levels of PAX9 (**Fig. 2C**). We found that both of these cell lines depend on PAX9 for cell viability and proliferation *in vitro* (**Fig. 2F–I**). This observation was further confirmed in a number of other ASCL1 positive (NCI-H69, NCI-H748) and negative (NCI-H196, NCI-H226, and NCI-H2171) cell lines (Supplementary Fig. S2G). To minimize the off-target effect of shRNAs, we also confirmed the results using the top two CRISPR gRNAs hits from the CRISPR screening in NCI-H1963 and NCI-H1882 cell lines (Supplementary Figs. S2H–S2J). Mechanistically, we found depletion of PAX9 dramatically induced the protein levels of phosphorylated histone H3S10 and reduced the protein levels of cyclin A2 (Supplementary Fig. S2K), indicating a potential function of PAX9 in the cell-cycle progression in SCLC cells. Indeed, consistent with the results from the *in vitro* experiment, we found depletion of PAX9 in mouse SCLC cell line KP1 (*p53/Rb* mutant) also significantly repressed tumor growth in animals (**Fig. 2J–L**).

Finally, we retrieved data from cBioPortal to determine whether PAX9 mRNA levels correlates with SCLC tumor stages (29). As shown in **Fig. 2M**, we have detected a remarkable increase of PAX9 expression in high-grade SCLC samples. To further determine the correlation between PAX9 and SCLC tumor stages at the protein level, we utilized an SCLC tissue microarray, which contains both normal lung tissue and malignant SCLC tumor samples to perform IHC staining. As a result, there were dramatically higher levels of PAX9 protein detected in malignant SCLC samples compared with normal lung tissues (**Fig. 2N**). In summary, 14 of 25 (56%) of stage I, II SCLC samples and 16 of 20 (80%) of stage III, IV SCLC samples have positive staining signals, whereas 1 of 5 (20%) of normal tissue is positive for PAX9 staining signals. In comparison with other types of lung cancer cell lines, SCLC cells tend to be more sensitive to PAX9 depletion (Supplementary Fig. S2L). All these results suggest that PAX9 can serve as a potential biomarker for human SCLC malignancy.

PAX9 marks enhancers of genes involved in neural function and differentiation

To determine the functions of PAX9 as a transcription factor in SCLC cells, we conducted ChIP-seq in NCI-H1963 cells with PAX9-specific antibody. In total, 6,847 PAX9-specific peaks were detected in two independent biological replicates (Pearson = 0.92), with more than 90% of PAX9 peaks annotated within intron and intergenic regions (**Fig. 3A**; Supplementary Fig. S3A). PAX9 peaks demonstrated enrichment in Nkx2.1, DLX5, Sox21, and PAX1 motifs, most of which are critical for lung tumorigenesis (**Fig. 3B**). To elucidate PAX9

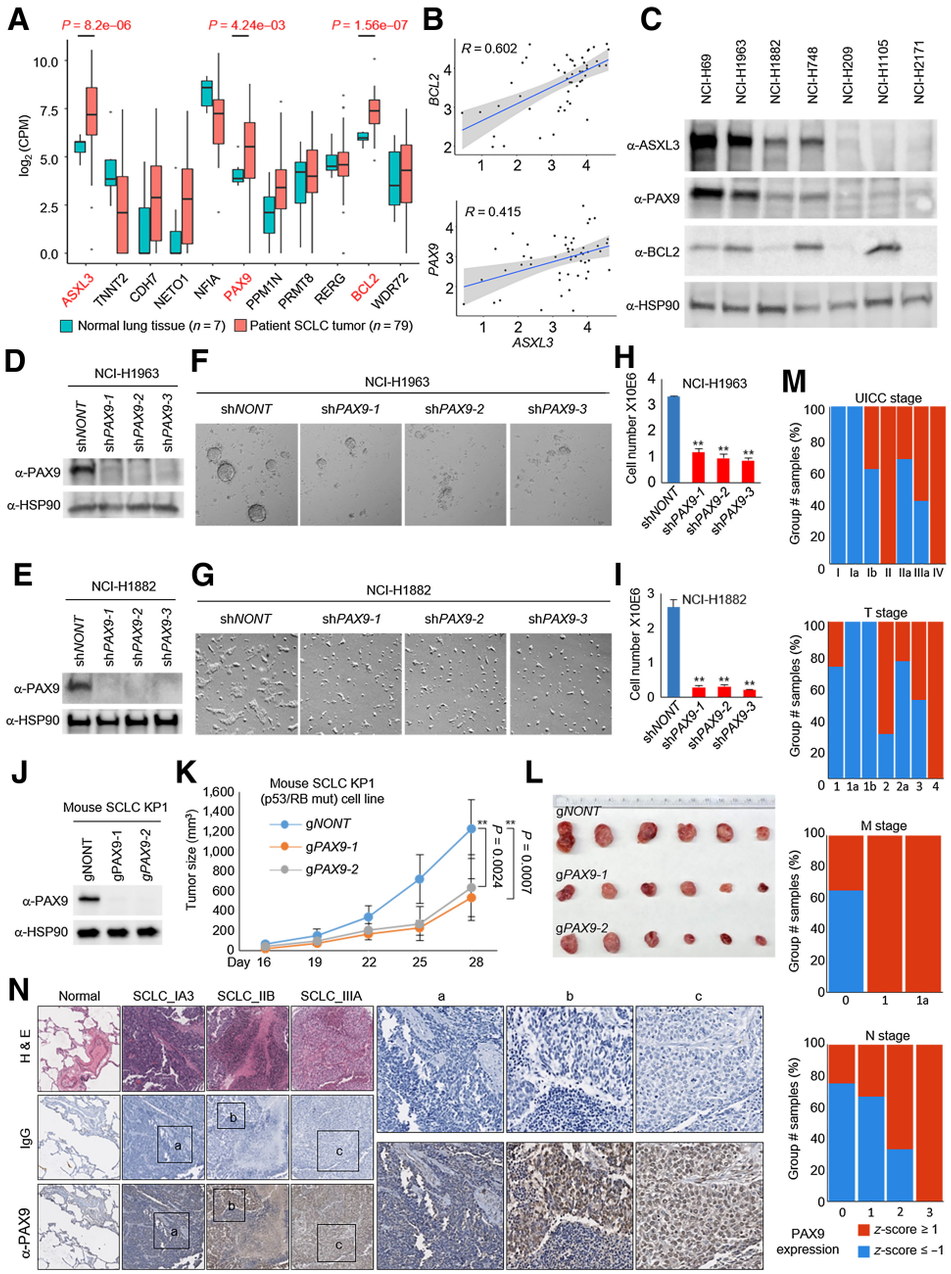

Figure 2.

PAX9 is a potential biomarker of SCLC and is required for SCLC viability. **A,** The RNA-seq data was retrieved from the GEO database (GSE60052), which contains the gene expression profiles of 7 normal lung tissue and 79 primary SCLC tissue samples. The box plot identified *ASXL3*, *BCL2*, and *PAX9* (red) with a significantly higher gene expression profile within tumor samples compared with normal tissue samples. The *P* value is calculated on the basis of the Welch two-sided *t* test. **B,** The scatter plot shows the correlation between *BCL2, PAX9*, and *ASXL3* gene expression within 50 human SCLC cell lines using the regression line and confidence interval analysis. *R* value represents the Pearson correlation coefficient. **C,** The Western blot shows protein levels of BCL2, PAX9, and ASXL3 in different SCLC cell lines. **D** and **E,** PAX9 protein levels were determined by Western blot in NCI-H1963 (**D**) and NCI-H1882 (**E**) cells transduced with either nontargeting shRNA or three distinct PAX9-specific shRNAs. **F** and **G,** Representative photographs showed the colony formation in NCI-H1963 (**F**) and NCI-H1882 (**G**) cells transduced with either nontargeting shRNA or PAX9-specific shRNAs. **H** and **I,** The cell number for each group was determined by cell counting assay. $n = 3$, two-tailed unpaired Student *t* test (**, $P < 0.01$). **J,** Mouse SCLC cell line KP1 was transduced with either nontargeting gRNA or two distinct PAX9-specific gRNA. The protein levels of PAX9 were determined by Western blot analysis. **K,** A total of 5.0×10^5 cells from each group in **J** were inoculated into the right flank of nude mice ($n = 6$). The tumor growth was measured every 3 days 2 weeks after the inoculation. A two-tailed unpaired Student *t* test was used for statistical analysis. **L,** Images for all tumor tissue from each mouse were taken at the end of the experiment. **M,** The RNA-seq data from 81 patients with SCLC were retrieved from cBioPortal. (data set from U cologne, Nature 2015; ref. 29). The mRNA expression *z* scores relative to all samples (log RNA-seq FPKM) were used to define the two groups with differential PAX9 expression (*z*-score ≥ 1 or *z*-score ⇐ −1 as the cutoff values). The PAX9 levels in each tumor stage category are shown. **N,** IHC staining of PAX9 in representative normal lung, SCLC_IB, SCLC_IIB, and SCLC_IIIA on the US Biomax BS04116a tissue microarray. IgG was used as a negative control. The hematoxylin and eosin (H&E) stain results were directly retrieved from US Biomax.

functions at enhancers, we divided PAX9 peaks into transcription start site (TSS) group and non-TSS group based on Homer annotation. The non-TSS group was further divided into two subgroups by K-means clustering. Then, we performed H3K4me1, H3K27ac, and H3K4me3 ChIP-seq experiments in NCI-H1963 SCLC cells, and centered the signals from each of the histone marks onto three clusters of PAX9 peaks to determine the enrichment of each histone modifications at PAX9 occupied loci (**Fig. 3C**).

It has been shown that enhancers are cell-type specific due to the existence of different epigenetic states, such as active, primed, or poised, based on the occupancy levels of H3K4me1, H3K27ac, and H3K27me3 (30). As shown in **Fig. 3C**, the non-TSS Cluster 1 (14% of total peaks) contains 971 peaks, which were enriched with higher levels of both H3K4me1 and H3K27ac signals compared with non-TSS Cluster 2 peaks (82% of total peaks), suggesting that peaks in Cluster 1 are enriched with active enhancers. Interestingly, in non-TSS Cluster 2, we also noticed that there still was a significant amount of PAX9 peaks with moderate levels of H3K4me1 but negligible levels of H3K27ac (**Fig. 3D** and **E**; Supplementary Fig. S3B). Furthermore, we performed the transposase accessible chromatin with high-throughput sequencing (ATAC-seq) experiment to determine the chromatin accessibility in each of PAX9 occupied clusters (**Fig. 3C** and **F**). Genome-wide analysis with our ATAC-seq data revealed a lower (but still significantly enriched) level of open chromatin at non-TSS Cluster 2 peaks, compared with TSS and non-TSS Cluster 1 peaks (**Fig. 3F** and **G**). The gene expression levels also correlated well with our defined clusters, with relatively higher expression levels in Cluster 1 than in Cluster 2 (Supplementary Fig. S3C). In addition, the box plot showed a very low enrichment of H3K27me3 levels at all PAX9-bound regions compared with H3K27me3-enriched loci (**Fig. 3H**), and there is also no detectable enrichment of PAX9 at H3K27me3 peaks and vice versa, suggesting that PAX9 is not an associated binding factor to poised (repressed) enhancer regions (**Fig. 3I** and **J**; Supplementary Fig. S3D). Overall, these results suggest that PAX9 preferentially binds and interacts with primed enhancers compared with active and poised enhancers.

Notably, genes occupied by PAX9 at TSS or close to PAX9 peaks at active enhancers (Cluster 1) are enriched for pathways that are fundamental, such as cell junction organization and signal transduction pathways, according to ChIPseeker and clusterProfiler analyses (**Fig. 3K**; Supplementary Figs. S3E and S3F). However, genes close to the Cluster 2 peaks enriched by primed enhancers are more involved with multiple neural-related pathways, such as the neuronal system, neurotransmitter receptors, and postsynaptic transmission pathways (**Fig. 3K**; Supplementary Fig. S3G). The representative track examples showed that PAX9 occupies at primed enhancers, which are enriched with H3K4me1 (but not H3K27ac) for several genes that are involved in the neural function and differentiation pathways, including *BDNF, DDX6, DNMT3B* (**Fig. 3L**), *CDH2*, and *MYCBP2* (Supplementary Fig. S3H). In summary, these results from our genome-wide studies provide an insight to a new potential role involving the association of PAX9 in controlling neural differentiation and neural gene expression in SCLC.

PAX9 functions as a transcriptional repressor in SCLC cells

To investigate whether PAX9 loss at enhancer regions can alter nearby genes' expression, we performed RNA-seq in cells transduced with either nontargeting shRNA (sh*NONT*) or two distinct PAX9 shRNAs to minimize off-target effects. As a result, a total of 1,026 genes were consistently downregulated, and a total of 1,089 genes were upregulated in PAX9-depleted cells (**Fig. 4A**). Interestingly, based on the GO pathway analysis, a number of neural-related pathways were enriched within the total upregulated vs. downregulated genes after PAX9 depletion (Supplementary Figs. S4A and S4B). To determine how PAX9 regulates gene expression at the transcription level, we integrated our RNA-seq data with PAX9 ChIP-seq analysis. We then examined the gene expression change surrounding PAX9 peaks at both non-TSS and TSS regions (**Fig. 4B**). As a result, majority of these genes with PAX9 occupancy are upregulated after PAX9 depletion (**Fig. 4B** and C). Interestingly, based on the GO pathway analysis, a handful of neural-related pathways were enriched among 244 of the upregulated genes after PAX9 depletion (**Fig. 4D**), compared with the 114 downregulated genes (Supplementary Fig. S4C). Overall, these results reveal a robust transcriptional repressive function of PAX9 in SCLC cells.

Gene set enrichment analysis (GSEA) was further introduced to determine the most significantly enriched pathways in PAX9-depleted cells. As a result, we found the gene signatures that are related to Polycomb-mediated transcription reprogramming, such as BMI_DN.V1_UP and PRC2_EZH2_UP.V1_DN, were significantly enriched in the upregulated genes in PAX9-depleted SCLC cells (**Fig. 4E**), and the gene signatures that are related to lung cancer development, such as KRAS.LUNG_Up.V1_DN and PTEN_DN.V1_DN, were significantly enriched in the upregulated genes within PAX9-depleted SCLC cells (Supplementary Fig. S4D). To determine whether the repressive transcriptional function of PAX9 is a general mechanism in different SCLC-A type cells, we knocked down PAX9 within three of the SCLC cell lines (NCI-H1963, NCI-H748, and NCI-H1882) with PAX9-specific shRNAs. Depletion of PAX9 induced a significant expression increase of *EPHB1, NGF, EBF2, MSX1*, and *CNTNAP2*, which indicated neural differentiation in different cell lines (**Fig. 4F**). Finally, to determine whether PAX9 plays a direct role in regulating transcriptional repression at those representative enhancer loci in **Fig. 4G**, the enhancer DNA (highlighted) were individually cloned into luciferase reporter constructs cotransfected with either GFP or GFP-tagged PAX9 in HEK293T cells (**Fig. 4H**). As a result, we observed a statistically significant amount of repressive transcriptional activity of PAX9 at these indicated loci (**Fig. 4I**).

The nucleosome remodeling deacetylase complex is required for PAX9-mediated transcriptional repression

To characterize the interactomes of PAX9 in cells, we stably expressed GFP and GFP-PAX9 in HEK293T cells (**Fig. 5A**) and purified GFP-tagged PAX9 proteins from benzonase-treated nuclear lysates with GFP purification as a negative control. By mass spectrometry analysis, we have identified 259 unique proteins that specifically interacted with GFP-tagged PAX9 but not GFP (Supplementary Fig. S5A). Pathway analysis with the 259 binding proteins revealed that multiple protein complexes involved in transcriptional regulation were coprecipitated with PAX9 (Supplementary Fig. S5A), such as the nucleosome remodeling deacetylase (NuRD) complex. The NuRD complex has been identified as a multi-subunit complex with both nucleosome remodeling and histone deacetylase activities (31), and participates in the establishment or maintenance of transcriptional repression at regions of the genome corresponding to highly methylated DNA (32). On the basis of our mass spectrometry analysis, we have been able to narrow it down by identifying components of the NuRD complex that are primary interactors with PAX9 in HEK293T cells (**Fig. 5B**). To validate our mass spectrometry result, we performed coimmunoprecipitation against GFP-tagged PAX9 and detected the interaction between PAX9 and several subunits within the NuRD complex, such as CHD4, HDAC1, and MTA1 (**Fig. 5C**). The copurification of endogenous HDAC1, HDAC2, LSD1, and

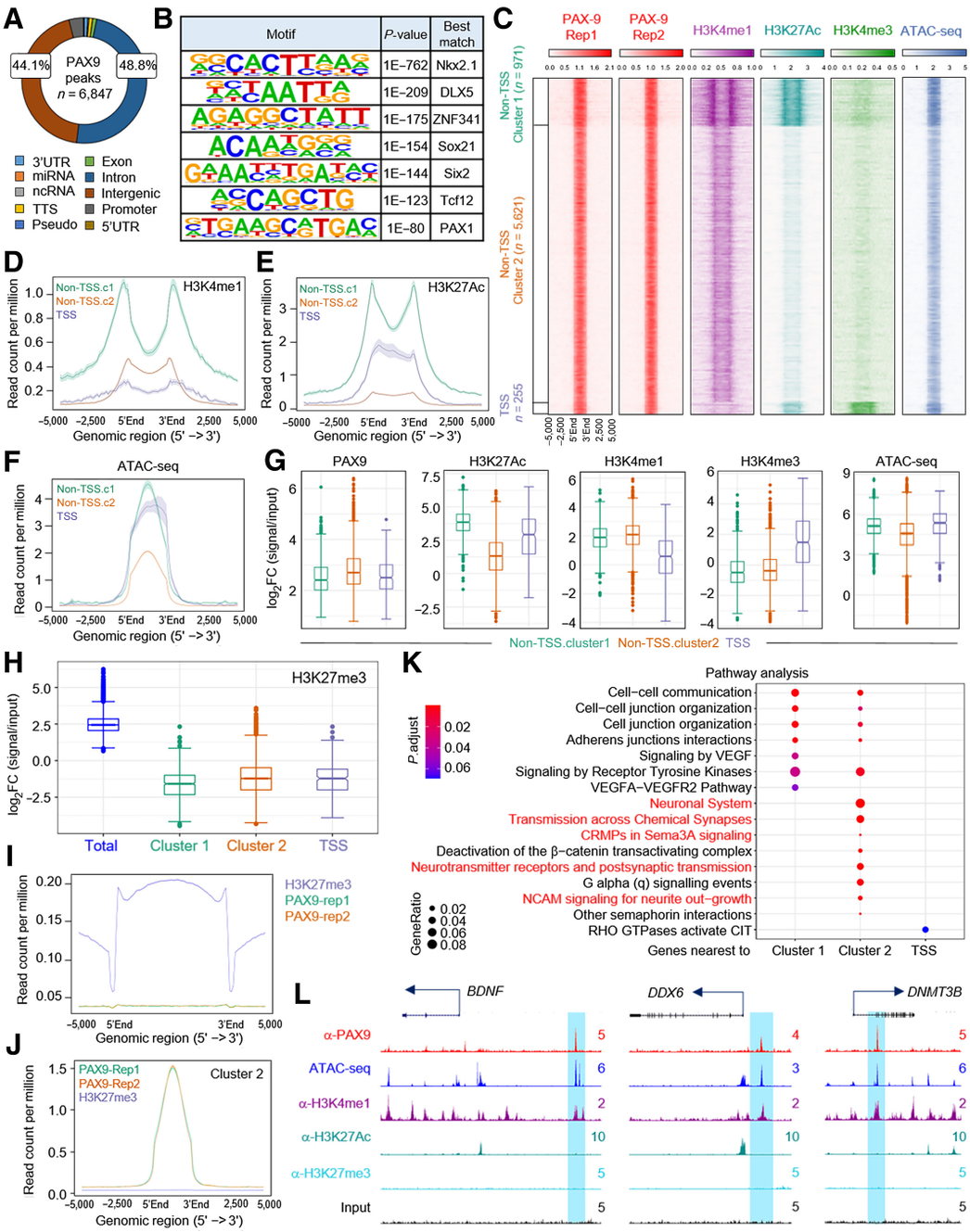

Figure 3.

PAX9 marks enhancers of genes involved in neural function and differentiation. **A,** Distribution of PAX9 binding to genomic regions in the human SCLC cell line NCI-H1963, as assessed by ChIP-seq. Peak annotation of PAX9 is summarized in a pie chart format. **B,** Motif enrichment analysis of the 6,847 specific PAX9 peaks from two independent biological replicates in NCI-H1963 cells. **C,** Heatmaps generated from ChIP-seq data analyses showed the occupancy of H3K4me1, H3K27ac, and H3K4me3 markers (left) and signals from ATAC-seq (right) in NCI-H1963 SCLC cells centered on the clustered PAX9 peaks. Non-TSS and TSS peaks were annotated with Homer annotation. Non-TSS peaks were then further divided into two clusters by k-means clustering (Cluster 1 and Cluster 2). **D–F,** The average plots showed the chromatin occupancy of H3K4me1 (**D**), H3K27ac (**E**), and chromatin accessibility (**F**) levels centered on PAX9 peaks of TSS, Cluster 1, and Cluster 2. **G,** The box plot shows the $\log_2$-fold change of PAX9, H3K4me1, H3K4me3, H3K27ac, and ATAC-seq signals versus input. **H,** The box plot shows the $\log_2$-fold change of total H3K27me3 and the enrichment of H3K27me3 levels on TSS, Cluster 1, and Cluster 2 peaks of PAX9 versus input. **I,** The average plots showed the chromatin occupancy of PAX9 levels centered on H3K27me3 peaks. **J,** The average plots showed the chromatin occupancy of H3K27me3 levels centered on PAX9 Cluster 2 peaks. **K,** Pathway analysis was performed using ChIPseeker with genes nearest to PAX9 Cluster 1, Cluster 2, and TSS peaks. **L,** Representative track examples show the occupancy of PAX9 at primed enhancers of *BDNF, DDX6*, and *DNMT3B* gene loci.

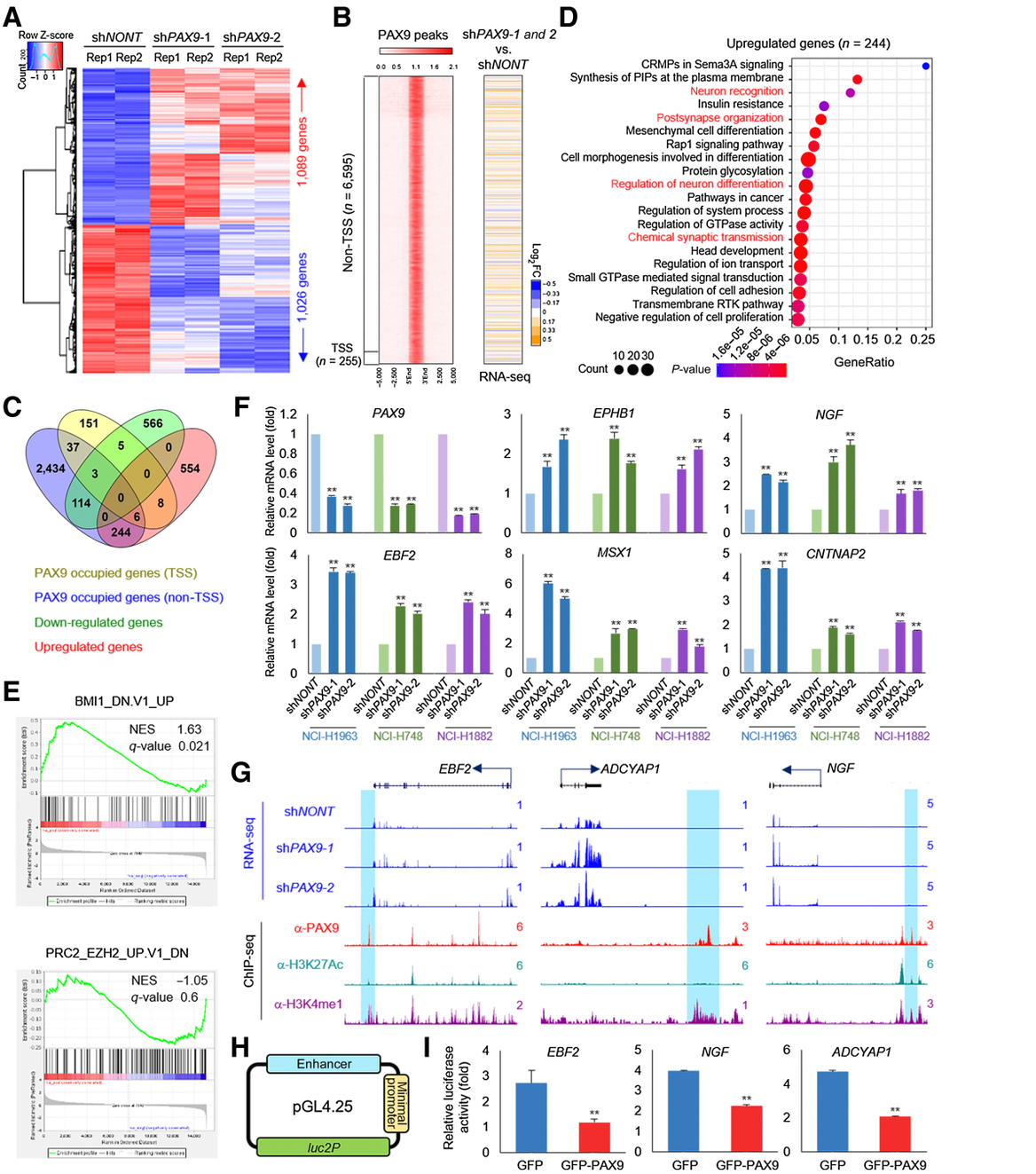

Figure 4.

PAX9 functions as a genome-wide transcription repressor. **A,** PAX9 was knocked down by two different shRNAs. RNA-seq was performed for NCI-H1963 cells transduced with nontargeting shRNA and two different ASXL3-specific shRNAs. Hierarchical clustering heatmaps showed all differentially expressed genes with ASXL3 knockdown. **B,** Heatmaps generated from ChIP-seq data analysis show the occupancy of PAX9 binding sites. Each row represents a unique PAX9 peak and the ChIP-seq signals of PAX9 were centered at PAX9 peaks and then further divided into TSS and non-TSS regions. The right panel shows the $\log_2$-fold change of nearby gene expression in NCI-H1963 cells transduced with nontargeting shRNA (sh*NONT*) or ASXL3-specific shRNAs. **C,** The Venn diagram identifies the direct transcriptional targets ($|\text{Log}_2\text{FC}| \geq 0.25$) of PAX9. **D** and **E,** Pathway analysis by Metascape (**D**) and GSEA (**E**) of genes that are occupied by PAX9, and upregulated and downregulated upon PAX9 depletion in NCI-H1963 cells. BMI1_DN.V1_UP, genes upregulated in DAOY cells (medulloblastoma) upon knockdown of *BMI1* gene by RNAi. PRC2_EZH2_UP.V1_DN, genes downregulated in TIG3 cells (fibroblasts) upon knockdown of *EZH2* gene. **F,** The mRNA levels of *PAX9, EBF2, EPHB1, NGF, MSX1*, and *CNTNAP2* were determined by real-time PCR in three different SCLC cell lines transduced with sh*NONT* or ASXL3-specific shRNAs. $n = 3$, two-tailed unpaired Student t test. **, $P < 0.01$. **G,** Representative tracks showing the enhancer binding of PAX9, which contributes to repressive gene expression. **H,** The enhancer regions highlighted in **G** were cloned into luciferase reporter vectors and cotransfected into HEK293T cells with either GFP or GFP-tagged PAX9. **I,** After 24 hours, cells were harvested, and luciferase activity was measured. Relative luciferase induction is plotted as a fold change based on cells transfected with empty reporter vectors. $n = 3$, two-tailed unpaired Student t test. **, $P < 0.01$.

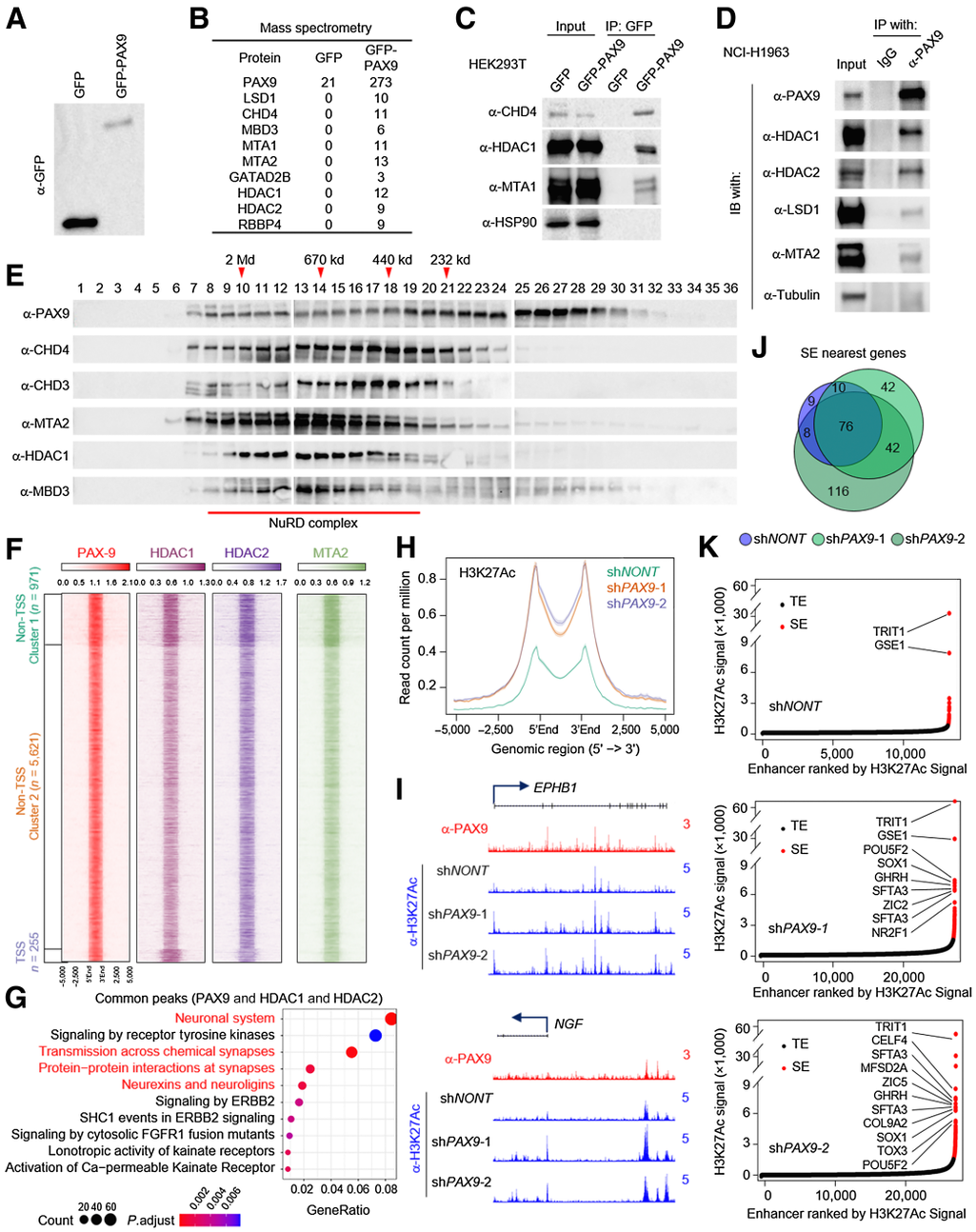

Figure 5.

The NuRD complex is required for PAX9-mediated transcriptional repression. **A,** HEK293T cells were infected by lentivirus expressing either GFP or GFP-tagged PAX9 and the protein levels of GFP or GFP-PAX9 were determined by Western blot analysis. **B,** The GFP-tagged proteins were purified from HEK293T cells and stably expressed either GFP or GFP-PAX9. The purified proteins were subjected to mass spectrometry analysis. Peptide numbers of the NuRD complex's subunits and PAX9 are shown. **C,** IP from whole cell lysates were performed with antibodies against the GFP epitope, followed by immunoblotting with antibodies against CHD4, HDAC1, and MTA1 in HEK293T cells transduced with either GFP or GFP-PAX9. HSP90 was used as a negative control. **D,** IP of endogenous PAX9 from NCI-H1963 cells followed by immunoblot (IB) for PAX9, HDAC1, HDAC2, LSD1, and MTA2. IgG was used as a negative control, $n = 2$. **E,** Nuclear extract from NCI-H1963 SCLC cells was subjected to size exclusion chromatography and then protein levels of PAX9, CHD3, CHD4, HDAC1, MTA2, and MBD3 were determined by Western blot analysis. $n = 2$. **F,** Heatmaps generated from ChIP-seq data analyses show the occupancy of HDAC1, HDAC2, and MTA2 in NCI-H1963 SCLC cells. ChIP-seq signals are centered on PAX9 peaks. **G,** Pathway analysis by Metascape with 4,004 common peaks among HDAC1, HDAC2, and PAX9. **H,** The average plot shows the chromatin occupancy of H3K27ac in NCI-H1963 cells transduced with either nontargeting shRNA or two distinct PAX9 shRNAs. **I,** Representative track examples show the H3K27ac levels at *EPHB1* and *NGF* gene loci in cells transduced with either nontargeting shRNA or PAX9 shRNAs. Histone H3 lysine 27 acetylation (H3K27ac) signals from ChIP sequencing identifies putative super enhancers in NCI-H1963 cells transduced with either nontargeting shRNA or two distinct PAX9 shRNAs. **J,** The Venn diagram shows the overlapped super enhancers (SE) between each group. **K,** Hockey stick plot representing the normalized rank and signals of H3K27ac. Representative of top-ranked super enhancer–associated genes from each group are labeled.

MTA2—subunits within the NuRD complex—along with PAX9 in SCLC cell line NCI-H1963 were also validated via Western blotting (**Fig. 5D**). Finally, to study the stoichiometry of endogenous PAX9 and the NuRD complex interaction, nuclear extracts from NCI-H1963 cells were subject to size exclusion chromatography, followed by Western blot analysis of the elution profile of PAX9, CHD3, CHD4, MTA2, HDAC1, and MBD3 (**Fig. 5E**). These studies indicated a significant proportion of PAX9 that co-eluted with most of the subunits from the NuRD complex at approximately 670 kDa.

To elucidate a possible cofunction between PAX9 and HDAC1/2, we conducted ChIP-seq for HDAC1, HDAC2, and MTA2 in NCI-H1963 cells. As shown in Supplementary Fig. S5B, a great portion of HDAC1/2 and MTA2 occupies intron and intergenic regions, similar to PAX9. Motif enrichment analysis with HDAC1/2 and MTA2 peaks indicated significant enrichment in NKX family and SOX family motifs (Supplementary Fig. S5C), which is also similar to PAX9 (**Fig. 3B**). Indeed, we found a significant amount of colocalization of HDAC1/2 and MTA2 with PAX9 when centered on the three clusters of PAX9 peaks (**Fig. 5F**). Collectively, there were 3,063 peaks that overlapped among PAX9, HDAC1, HDAC2, and MTA2 (Supplementary Fig. S5D). Intriguingly, majority of these overlapped peaks localized at other intron and distal intergenic regions (Supplementary Fig. S5E) and were enriched with genes involved in the neural system and various neural function pathways (**Fig. 5G**).

To determine the impact of PAX9 on the H3K27ac deacetylase activity of both HDAC1 and HDAC2, we compared the H3K27ac levels between cells transduced with either nontargeting shRNA or PAX9-specific shRNAs by ChIP-seq and genome-wide analyses. As a result, we found a dramatic increase of H3K27ac levels at PAX9 loci after PAX9 depletion (**Fig. 5H** and **I**). Consistent with this result, depletion of PAX9 leads to a dramatic reduction of chromatin bound HDAC1/2 at a subset of PAX9 and HDAC1 or HDAC2 co-occupied regions, suggesting a potential role of PAX9 in mediating the NuRD complex recruitment to chromatin (Supplementary Fig. S5F). Finally, we compared the super-enhancer (SE)-associated genes between NCI-H1963-sh*NONT* and NCI-H1963-sh*PAX9*, based on the ranking of H3K27ac ChIP-seq signals. Depletion of PAX9 by two distinct shRNAs led to a discovery of 42 new super-enhancers within SCLC cells (**Fig. 5J** and K). In summary, these results suggest a potential cofunction between PAX9 and the NuRD complex with their involvement in repressing enhancer activity and gene expression among SCLC cells.

Pharmaceutical inhibition of HDAC abrogates PAX9-mediated transcriptional repression

To determine whether inhibition of the catalytic activity of HDAC1/2 could rescue the expression of PAX9 target genes, we treated NCI-H1963 cells with an HDAC1/2 selective inhibitor MERCK60 for 24 hours (**Fig. 6A**), whereas the 4-day EZH2 inhibitor treatment (GSK126) was used as a control (**Fig. 6B**). As a result, we found both inhibitors could efficiently induce histone modification changes in NCI-H1963 cells. Then we conducted RNA-seq to determine the transcriptional profile of cells treated with DMSO and the HDAC inhibitor or EZH2 inhibitor. As shown in **Fig. 6C**, we found more than half of PAX9 repressed genes (170/337, $\log_2$FC > 0.5), such as tumor suppressive gene *NGF* (33), *CDH4* (34), *PTPRM* (35), *FEZ1* (36), *DOCK4* (37), and *MSX1* (38), were significantly rescued by HDAC inhibitor treatment, whereas the EZH2 inhibitor could only rescue 47 genes. A box-plot analysis of Log2 fold change gene expression of common-upregulated genes identified from the two distinct PAX9 shRNAs in NCI-H1963 cells were also affected by MERCK60 treatment (**Fig. 6D**). In addition, pathway analysis revealed that regulation of neural differentiation pathway was the most significantly enriched pathway identified by the 170 PAX9 target genes that could be re-elevated by HDAC inhibitor treatment (Supplementary Fig. S6A). Then, we integrated the RNA-seq data with PAX9 ChIP-seq analysis and found that the HDAC inhibitor (but not EZH2 inhibitor) could induce the re-expression of genes that are occupied by PAX9 at primed enhancers within the non-TSS Cluster 2 group (**Fig. 6E**, left, **and F**), along with a concomitant increase of histone H3K27ac levels (**Fig. 6E**, right). We further validated the RNA-seq data with real-time PCR and found that most of the neural differentiation genes that are repressed by PAX9 can be rescued upon HDAC inhibitor treatment (**Fig. 6G**; Supplementary Fig. S6B). Intriguingly, the H3K27ac levels at PAX9-dependent primed enhancers were significantly increased upon HDAC inhibitor treatment (**Fig. 6H–J**), which is similar to PAX9 depletion (Supplementary Fig. S6C). HDAC inhibitors have been shown to alter histone acetylation levels and reduce tumor growth *in vivo* (39). However, in human SCLC clinical trials, HDAC inhibitors have not shown an objective response in patients with chemo-sensitive SCLC (40). These results suggest a need for a more personalized therapeutic approach, which requires identifying and utilizing functional predictive biomarkers that can significantly improve SCLC outcomes. To determine whether the expression level of PAX9 is a determinant of responsiveness to HDAC inhibitor, we selected four SCLC cell lines with different PAX9 expression levels and treated them with the HDAC inhibitor MERCK60 *in vitro*. As a result, we found that treatment with MERCK60 could induce a significant increase in H3K27ac levels for all four cell lines (**Fig. 6K**). NCI-H748 and NCI-H1963 cells, which express high levels of ASXL3 and PAX9, are more sensitive to HDAC inhibitor treatment than those two other low expressing cell lines (**Fig. 6L**). Moreover, the drug sensitivity trend was also observed and shown to be consistent with other SCLC cell lines expressing both high and low levels of ASXL3 and PAX9 (Supplementary Figs. S6D and S6E). Finally, we asked whether the cells expressing high levels of PAX9 are also sensitive to depletion of the catalytic core subunit CHD4 within the NuRD complex. As a result, we found depletion of CHD4 with two distinct CRISPR gRNAs could significantly reduce cell growth *in vitro* (Supplementary Figs. S6F and S6G). In summary, these results reveal a potential therapeutic strategy by targeting the NuRD complex for patients with SCLC with a highly expressed PAX9 phenotype (**Fig. 6M**).

Discussion

ASXL3 is a tissue-specific additional sex comb-like protein and plays an essential function in the human nervous system (41). On the basis of our previous research findings and other groups' combined results, ASXL3 is critical for human SCLC cell viability, both *in vitro* and *in vivo* (23). We have further characterized the function of a novel epigenetic axis involving interactions with BAP1, ASXL3, and BRD4 at active enhancers in human SCLC cells (20). However, how ASXL3 maintains SCLC cell viability and determines cell fate remains to be uncovered.

To circumvent the difficulty generating stable ASXL3-KO cells due to the lethal nature of complete depletion of ASXL3 in SCLC cells, we alternatively introduced two lung cancer cell lines with different ASXL3 levels for the CRISPR-Cas9 dropout screening in our current studies. By comparing RNA-seq data generated from ASXL3 wild-type with knockdown cells, we were able to identify a specific 10-gene signature that is essential for ASXL3-highly expressed cell viability. However, based on the RNA-seq results from primary patient-derived

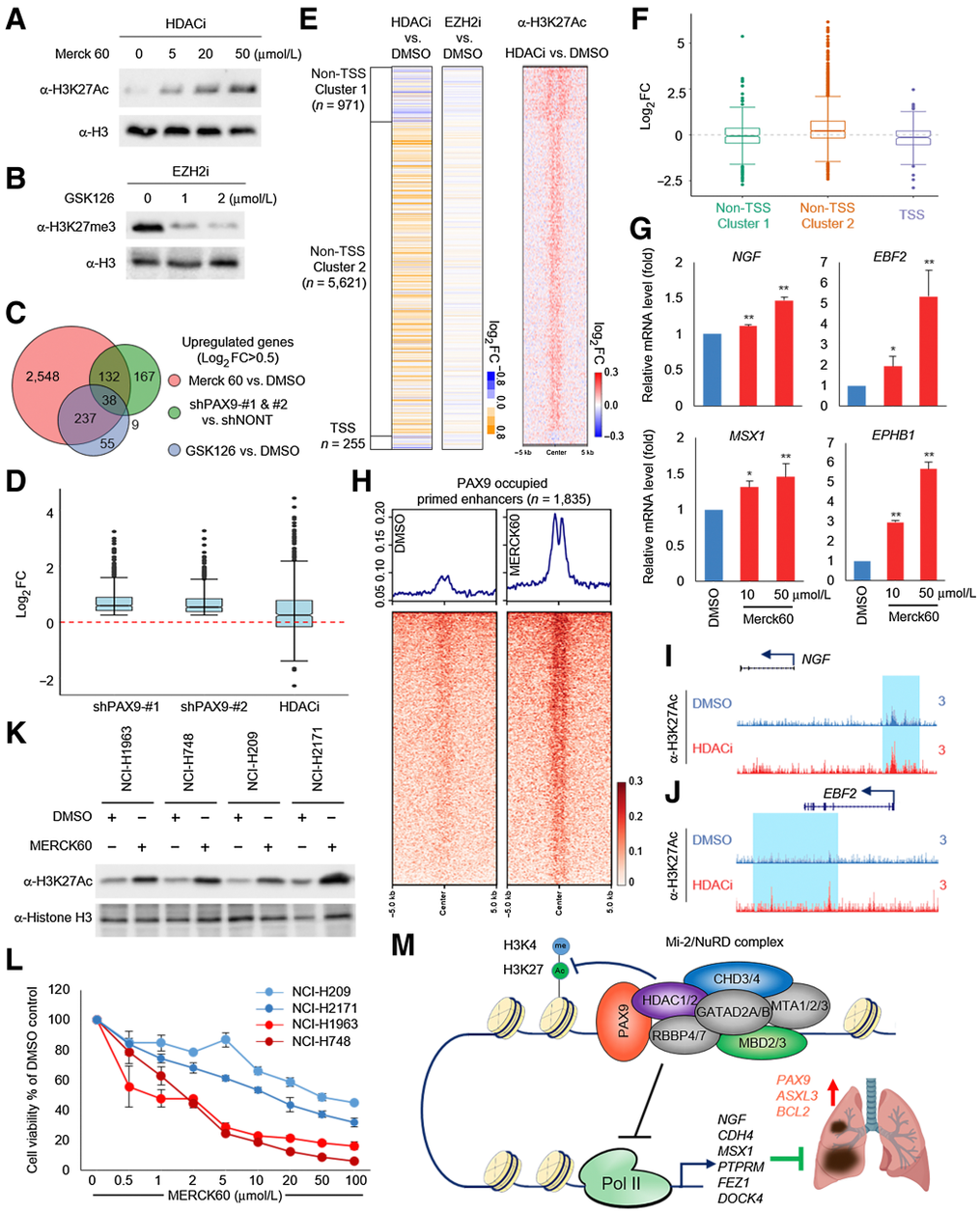

Figure 6.

Pharmaceutical inhibition of HDAC abrogates PAX9-mediated transcriptional repression. NCI-H1963 cells were treated with different concentrations of HDAC inhibitor MERCK60 (selective for HDAC1 and HDAC2) for 24 hours or EZH2 inhibitor GSK126 for 96 hours. **A** and **B,** The protein levels of H3K27ac (**A**) and H3K27me3 (**B**) were determined by Western blot analysis. **C,** The Venn diagram shows the overlap of upregulated genes among PAX9 depletion, MERCK60, and GSK126 treatments. **D,** Common upregulated genes with two distinct PAX9 shRNAs in NCI-H1963 cell line (adj. $P < 0.01$, $\log_2FC > 0.25$) were extracted. The box plot shows this group of gene expression change with PAX9 knockdown and MERCK60 treatment ($n = 805$). The expression count is $\log_2$ (FPKM+1) transformed. Red dashed line, no change. **E,** Left, the heatmaps show the $\log_2$-fold change of nearby gene expression in NCI-H1963 cells treated with DMSO, HDAC inhibitor MERCK60, or EZH2 inhibitor GSK126. Right, the $\log_2$-fold change of H3K27ac levels is shown. **F,** The box plot shows gene expression changes with MERCK60 treatment in NCI-H1963 cell line among three clusters defined in **E**. The expression count is $\log_2$ (FPKM+1) transformed. **G,** NCI-H1963 cells were treated with MERCK60 for 24 hours. The mRNA levels of *NGF, EBF2, EPHB1*, and *MSX1* were determined by real-time PCR. $n = 3$, two-tailed unpaired Student t test. *, $P < 0.05$; **, $P < 0.01$. **H–J,** The heatmap (**H**) and track examples (**I** and **J**) show the H3K27ac levels at PAX9 occupied primed enhancers before (DMSO) and after MERCK60 treatment. **K,** Four different human SCLC cell lines, NCI-H748, NCI-H1963, NCI-H209, and NCI-H2171, were treated with MERCK60 for 24 hours. The protein levels of H3K27ac were determined by Western blot analysis. **L,** The cell viability of each cell line from **K** was determined by CellTiter-Glo Cell Viability Assay after 72-hour treatment of different concentrations of MERCK60. $n = 3$. **M,** The model shows how elevated ASXL3 in SCLC cells increases cell viability by driving a 10-gene signature, such as *PAX9* and *BCL2*. PAX9 cooperates with the NuRD complex at primed enhancers to repress normal neural function genes such as *NGF, MSX1*, and *ADCYAP1*, many of which, function as tumor suppressors in SCLC. Upon HDAC inhibition, expression of functional genes related to neural differentiation was re-elevated to suppress cell growth.

SCLC samples and normal lung tissue, not all of the genes within the 10-gene signature were significantly elevated in tumor samples, except for *BCL2* and *PAX9*. PAX9 is a lineage-specific transcription factor, and has been linked to tumorigenesis (42–44). In human lung cancer, a discovery was made with identifying a recurrent lung cancer amplicon located at 14q13.3, which contains three genes in the core region (*NKX2.1, NKX2.8*, and *PAX9*). Overexpression of PAX9 with either Nkx2.1 or Nkx2.8 showed pronounced synergy in promoting the proliferation of immortalized human lung epithelial cells. Although we have not detected an increase of Nkx2.1/Nkx2.8 expression in SCLC patient samples, based on our motif analysis shown in **Fig. 3B**, Nkx2.1 and PAX9 both share very similar DNA binding motifs, suggesting there might be a critical role in the involvement of PAX9/Nkx2.1 in lung tumorigenesis (45, 46).

Surprisingly, as a transcription factor, we found less than 7% of PAX9 occupies the promoter/TSS regions at the chromatin in SCLC cells. Instead, the vast majority (more than 92%) of PAX9 occupies distal regulatory elements in SCLC cells, pointing to the role of PAX9 as an enhancer-specific binding factor in SCLC. Enhancers play a crucial role in driving gene expression and can activate targeted genes from great distances (47, 48). Enhancers can exist in various epigenetic states, including active, primed, or poised. Poised enhancers are marked by H3K4me1 and H3K27me3 histone marks. Primed enhancers are marked by histone H3 lysine 4 (H3K4) mono/di-methylation (H3K4me1/2), whereas active enhancers are then further marked by H3K27 acetylation (H3K27ac; ref. 30).

In our current studies, we have uncovered a novel role of PAX9 functions as transcriptional repressor that restricts enhancer activity and maintains the primed status of enhancers in human SCLC cells, leading to a strong repression of numerous neural differentiation genes and tumor suppressors. These results lead us to further investigate the mechanism as to how PAX9 represses gene expression at enhancers. On the basis of our PAX9 purification and mass spectrometry analysis, we identified the NuRD Complex as one of the top interactors of PAX9, which has been identified as a transcriptional repressor across different cell types. Consequently, genetic depletion of PAX9 leads to an increase of H3K27ac levels at enhancer loci, similar to HDAC1/2 inhibitor treatment. Notably, we did not observe any significant hits for the NuRD complex in our genome-wide CRISPR-Cas9 screening. This is probably due to there being different compositions of the NuRD complex, and also some of these subunits have redundant roles as shown in biochemistry and genetic studies (49). Thus, depletion of a single subunit may not fully impair the function of the whole complex.

Emerging studies have shown the oncogenic function of BAP1 in different types of cancer. In our previous studies, we have detected a dramatic cofunction between BAP1 and ASXL3 in SCLC cells (20). In mutant ASXL1-driven leukemia models, inhibition of BAP1 by small molecule inhibitors could significantly reduce tumor burden and extend animal survival (50). Because PAX9 is a direct transcriptional target of the BAP1/ASXL3/BRD4 epigenetic axis, our studies have raised the possibility of targeting BAP1 activity for lung cancer treatment.

Authors' Disclosures

B.D. Singer reports grants from NIH during the conduct of the study. E.T. Bartom reports grants from NIH during the conduct of the study and grants from NIH outside the submitted work. No disclosures were reported by the other authors.

Authors' Contributions

Z. Zhao: Data curation, software. **A.P. Szczepanski:** Data curation, validation, investigation, methodology. **N. Tsuboyama:** Data curation, validation. **H. Abdala-Valencia:** Data curation, investigation. **Y.A. Goo:** Investigation. **B.D. Singer:** Investigation. **E.T. Bartom:** Data curation, investigation. **F. Yue:** Software, supervision. **L. Wang:** Conceptualization, resources, data curation, software, formal analysis, supervision, funding acquisition, validation, investigation, visualization, methodology, writing–original draft, project administration, writing–review and editing.

Acknowledgments

The authors would like to thank the following: Dr. Julien Sage for the kind gifts of mouse small cell lung cancer cell lines KP1 and KP3, and Dr. Feng Zhang for the kind gifts of the Px330 and lentiCRISPR v2 vectors. Dr. Benjamin D. Singer was supported by NIH/NHLBI awards R01HL149883 and R01HL153122. Proteomics services were performed by the Northwestern Proteomics Core Facility, generously supported by NCI CCSG P30 CA060553 awarded to the Robert H. Lurie Comprehensive Cancer Center, instrumentation award (S10OD025194) from NIH Office of Director, and the National Resource for Translational and Developmental Proteomics supported by P41 GM108569.

The publication costs of this article were defrayed in part by the payment of publication fees. Therefore, and solely to indicate this fact, this article is hereby marked "advertisement" in accordance with 18 USC section 1734.

Note

Supplementary data for this article are available at Cancer Research Online (http://cancerres.aacrjournals.org/).

Received April 9, 2021; revised July 1, 2021; accepted July 28, 2021; published first August 2, 2021.

References

1. Torre LA, Bray F, Siegel RL, Ferlay J, Lortet-Tieulent J, Jemal A. Global cancer statistics, 2012. CA Cancer J Clin 2015;65:87–108.
2. Miller KD, Nogueira L, Mariotto AB, Rowland JH, Yabroff KR, Alfano CM, et al. Cancer treatment and survivorship statistics, 2019. CA Cancer J Clin 2019;69:363–85.
3. Gazdar AF, Bunn PA, Minna JD. Small-cell lung cancer: what we know, what we need to know and the path forward. Nat Rev Cancer 2017;17:725–37.
4. Gardner EE, Lok BH, Schneeberger VE, Desmeules P, Miles LA, Arnold PK, et al. Chemosensitive relapse in small cell lung cancer proceeds through an EZH2-SLFN11 Axis. Cancer Cell 2017;31:286–99.
5. Rudin CM, Poirier JT, Byers LA, Dive C, Dowlati A, George J, et al. Molecular subtypes of small cell lung cancer: a synthesis of human and mouse model data. Nat Rev Cancer 2019;19:289–97.
6. Amelung JT, Buhrens R, Beshay M, Reymond MA. Key genes in lung cancer translational research: a meta-analysis. Pathobiology 2010;77:53–63.
7. Augustyn A, Borromeo M, Wang T, Fujimoto J, Shao C, Dospoy PD, et al. ASCL1 is a lineage oncogene providing therapeutic targets for high-grade neuroendocrine lung cancers. Proc Natl Acad Sci USA 2014;111:14788–93.
8. Mollaoglu G, Guthrie MR, Bohm S, Bragelmann J, Can I, Ballieu PM, et al. MYC drives progression of small cell lung cancer to a variant neuroendocrine subtype with vulnerability to aurora kinase inhibition. Cancer Cell 2017;31:270–85.
9. Borromeo MD, Savage TK, Kollipara RK, He M, Augustyn A, Osborne JK, et al. ASCL1 and NEUROD1 reveal heterogeneity in pulmonary neuroendocrine tumors and regulate distinct genetic programs. Cell Rep 2016;16:1259–72.
10. Castro DS, Martynoga B, Parras C, Ramesh V, Pacary E, Johnston C, et al. A novel function of the proneural factor Ascl1 in progenitor proliferation identified by genome-wide characterization of its targets. Gene Dev 2011;25:930–45.
11. Schaffer BE, Park KS, Yiu G, Conklin JF, Lin CW, Burkhart DL, et al. Loss of p130 accelerates tumor development in a mouse model for human small-cell lung carcinoma. Cancer Res 2010;70:3877–83.

12. Plass C, Pfister SM, Lindroth AM, Bogatyrova O, Claus R, Lichter P. Mutations in regulators of the epigenome and their connections to global chromatin patterns in cancer. Nat Rev Genet 2013;14:765–80.
13. Wang L, Zhao ZB, Ozark PA, Fantini D, Marshall SA, Rendleman EJ, et al. Resetting the epigenetic balance of Polycomb and COMPASS function at enhancers for cancer therapy. Nat Med 2018;24:758–69.
14. Wang L, Shilatifard A. UTX mutations in human cancer. Cancer Cell 2019;35: 168–76.
15. Carbone M, Yang HN, Pass HI, Krausz T, Testa JR, Gaudino G. BAP1 and cancer. Nat Rev Cancer 2013;13:153–9.
16. Ley TJ, Ding L, Walter MJ, McLellan MD, Lamprecht T, Larson DE, et al. DNMT3A mutations in acute myeloid leukemia. N Engl J Med 2010;363: 2424–33.
17. Rasmussen KD, Jia GS, Johansen JV, Pedersen MT, Rapin N, Bagger FO, et al. Loss of TET2 in hematopoietic cells leads to DNA hypermethylation of active enhancers and induction of leukemogenesis. Gene Dev 2015;29:910–22.
18. Dhar SS, Zhao DY, Lin T, Gu BN, Pal K, Wu SJ, et al. MLL4 is required to maintain broad H3K4me3 peaks and super-enhancers at tumor suppressor genes. Mol Cell 2018;70:825–41.
19. Gao YN, Geng JS, Hong X, Qi JP, Teng Y, Yang Y, et al. Expression of p300 and CBP is associated with poor prognosis in small cell lung cancer. Int J Clin Exp Patho 2014;7:760–7.
20. Szczepanski AP, Zhao ZB, Sosnowski T, Goo YA, Bartom ET, Wang L. ASXL3 bridges BRD4 to BAP1 complex and governs enhancer activity in small cell lung cancer. Genome Med 2020;12:63.
21. Sanjana NE, Shalem O, Zhang F. Improved vectors and genome-wide libraries for CRISPR screening. Nat Methods 2014;11:783–4.
22. Wang L, Zhao Z, Meyer MB, Saha S, Yu M, Guo A, et al. CARM1 methylates chromatin remodeling factor BAF155 to enhance tumor progression and metastasis. Cancer Cell 2014;25:21–36.
23. Shukla V, Rao M, Zhang HG, Beers J, Wangsa D, Wangsa D, et al. ASXL3 is a novel pluripotency factor in human respiratory epithelial cells and a potential therapeutic target in small cell lung cancer. Cancer Res 2017;77:6267–81.
24. Li W, Xu H, Xiao TF, Cong L, Love MI, Zhang F, et al. MAGeCK enables robust identification of essential genes from genome-scale CRISPR/Cas9 knockout screens. Genome Biol 2014;15:554.
25. Jiang L, Shen HB, Yao YH. Genomic landscape survey identifies SRSF1 as a key oncodriver in small cell lung cancer. Chest 2016;149:328a.
26. Ghandi M, Huang FW, Jane-Valbuena J, Kryukov GV, Lo CC, McDonald ER, et al. Next-generation characterization of the Cancer Cell Line Encyclopedia. Nature 2019;569:503–8.
27. Etchegaray JP, Zhong L, Li C, Henriques T, Ablondi E, Nakadai T, et al. The histone deacetylase SIRT6 restrains transcription elongation via promoter-proximal pausing. Mol Cell 2019;75:683–99.
28. Wyce A, Ganji G, Smitheman KN, Chung CW, Korenchuk S, Bai YC, et al. BET inhibition silences expression of MYCN and BCL2 and induces cytotoxicity in neuroblastoma tumor models. PLoS One 2013;8:e72967.
29. George J, Lim JS, Jang SJ, Cun Y, Ozretic L, Kong G, et al. Comprehensive genomic profiles of small cell lung cancer. Nature 2015;524:47–53.
30. Calo E, Wysocka J. Modification of enhancer chromatin: what, how, and why? Mol Cell 2013;49:825–37.
31. Zhang Y, Ng HH, Erdjument-Bromage H, Tempst P, Bird A, Reinberg D. Analysis of the NuRD subunits reveals a histone deacetylase core complex and a connection with DNA methylation. Gene Dev 1999;13:1924–35.
32. Denslow SA, Wade PA. The human Mi-2/NuRD complex and gene regulation. Oncogene 2007;26:5433–8.
33. Missale C, Codignola A, Sigala S, Finardi A, Paez-Pereda M, Sher E, et al. Nerve growth factor abrogates the tumorigenicity of human small cell lung cancer cell lines. Proc Natl Acad Sci U S A 1998;95:5366–71.
34. Li Z, Su D, Ying L, Yu G, Mao W. Study on expression of CDH4 in lung cancer. World J Surg Oncol 2017;15:26.
35. Wang F, Liu DB, Zhao Q, Chen G, Liu XM, Wang YN, et al. The genomic landscape of small cell carcinoma of the esophagus. Cell Res 2018;28: 771–4.
36. Nonaka D, Fabbri A, Roz L, Mariani L, Vecchione A, Moore GW, et al. Reduced FEZ1/LZTS1 expression and outcome prediction in lung cancer. Cancer Res 2005;65:1207–12.
37. Yajnik V, Paulding C, Sordella R, McClatchey AI, Saito M, Wahrer DC, et al. DOCK4, a GTPase activator, is disrupted during tumorigenesis. Cell 2003;112: 673–84.
38. Yue Y, Zhou K, Li J, Jiang S, Li C, Men H. MSX1 induces G_0-G_1 arrest and apoptosis by suppressing Notch signaling and is frequently methylated in cervical cancer. Onco Targets Ther 2018;11:4769–80.
39. Marks PA, Richon VM, Rifkind RA. Histone deacetylase inhibitors: inducers of differentiation or apoptosis of transformed cells. J Natl Cancer Inst 2000;92: 1210–6.
40. Otterson GA, Hodgson L, Pang H, Vokes EE, Cancer L, Group B. Phase II study of the histone deacetylase inhibitor Romidepsin in relapsed small cell lung cancer (Cancer and Leukemia Group B 30304). J Thorac Oncol 2010;5: 1644–8.
41. Srivastava A, Ritesh KC, Tsan YC, Liao R, Su FY, Cao XH, et al. De novo dominant ASXL3 mutations alter H2A deubiquitination and transcription in Bainbridge-Ropers syndrome. Hum Mol Genet 2016;25:597–608.
42. Talukdar FR, Lima SCS, Khoueiry R, Laskar RS, Cuenin C, Sorroche BP, et al. Genome-Wide DNA methylation profiling of esophageal squamous cell carcinoma from global high-incidence regions identifies crucial genes and potential cancer markers. Cancer Res 2021;81:2612–24.
43. Xiong ZH, Ren S, Chen H, Liu Y, Huang CZ, Zhang YL, et al. PAX9 regulates squamous cell differentiation and carcinogenesis in the oro-oesophageal epithelium. J Pathol 2018;244:164–75.
44. Rani L, Mathur N, Gupta R, Gogia A, Kaur G, Dhanjal JK, et al. Genome-wide DNA methylation profiling integrated with gene expression profiling identifies PAX9 as a novel prognostic marker in chronic lymphocytic leukemia. Clin Epigenetics 2017;9:57.
45. Kendall J, Liu Q, Bakleh A, Krasnitz A, Nguyen KCQ, Lakshmi B, et al. Oncogenic cooperation and coamplification of developmental transcription factor genes in lung cancer. P Natl Acad Sci USA 2007;104:16663–8.
46. Hsu DS, Acharya CR, Balakumaran BS, Riedel RF, Kim MK, Stevenson M, et al. Characterizing the developmental pathways TTF-1, NKX2-8, and PAX9 in lung cancer. P Natl Acad Sci USA 2009;106:5312–7.
47. Creyghton MP, Cheng AW, Welstead GG, Kooistra T, Carey BW, Steine EJ, et al. Histone H3K27ac separates active from poised enhancers and predicts developmental state. P Natl Acad Sci USA 2010;107:21931–6.
48. Heintzman ND, Hon GC, Hawkins RD, Kheradpour P, Stark A, Harp LF, et al. Histone modifications at human enhancers reflect global cell-type-specific gene expression. Nature 2009;459:108–12.
49. Jurkin J, Zupkovitz G, Lagger S, Grausenburger R, Hagelkruys A, Kenner L, et al. Distinct and redundant functions of histone deacetylases HDAC1 and HDAC2 in proliferation and tumorigenesis. Cell Cycle 2011;10:406–12.
50. Wang L, Birch NW, Zhao ZB, Nestler CM, Kazmer A, Shilati A, et al. Epigenetic targeted therapy of stabilized BAP1 in ASXL1 gain-of-function mutated leukemia. Nat Cancer 2021;2:515–26.